



Absolute Calibration method for FMCW Cloud Radars

Felipe Toledo¹, Julien Delanoë², Martial Haeffelin³, and Jean-Charles Dupont⁴

¹Laboratoire de Météorologie Dynamique, École Polytechnique, Institut Polytechnique de Paris, 91128 Palaiseau, France

²Laboratoire Atmosphères, Milieux, Observations Spatiales/UVSQ/CNRS/UPMC, 78280 Guyancourt, France

³Institut Pierre Simon Laplace, École Polytechnique, CNRS, Institut Polytechnique de Paris, 91128 Palaiseau, France

⁴Institut Pierre-Simon Laplace, École Polytechnique, UVSQ, Université Paris-Saclay, 91128 Palaiseau, France

Correspondence: Felipe Toledo (ftoledo@lmd.polytechnique.fr)

Abstract.

This article presents a new Cloud Radar calibration methodology using solid reference reflectors mounted on masts, developed during two field experiments held in 2018 and 2019 at the SIRTAs atmospheric observatory, located in Palaiseau, France, in the framework of the ACTRIS-2 research and innovation program.

5 The experimental setup includes 10 cm and 20 cm triangular trihedral targets installed at the top of 10 m and 20 m masts, respectively. The 10 cm target is mounted on a pan-tilt motor at the top of the 10 m mast to precisely align its boresight with the radar beam. Sources of calibration bias and uncertainty are identified and quantified. Specifically, this work assesses the impact of receiver compression, incomplete antenna overlap, temperature variations inside the radar, clutter and experimental setup misalignment. Setup misalignment is a source of bias previously undocumented in the literature, that can have an impact
10 on the order of tenths of dB in calibration retrievals of W band Radars.

A detailed analysis enabled the design of a calibration methodology which can reach a cloud radar calibration uncertainty of 0.3 dB based on the equipment used in the experiment. Among different sources of uncertainty, the two largest terms are due to signal-to-clutter ratio and radar-to-target alignment. The analysis revealed that our 20 m mast setup with an approximate alignment approach is preferred to the 10 m mast setup with the motor-driven alignment system. The calibration uncertainty
15 associated with signal-to-clutter ratio of the former is ten times smaller than for the latter.

Cloud radar calibration results are found to be repeatable when comparing results from a total of 18 independent tests. Once calibrated the cloud radar provides valid reflectivity values when sampling mid-tropospheric clouds. Thus we conclude that the method is repeatable and robust, and that the uncertainties are precisely characterized. The method can be implemented under different configurations as long as the proposed principles are respected. It could be extended to reference reflectors held by
20 other lifting devices such as tethered balloons or unmanned aerial vehicles.

1 Introduction

Clouds remain to this day one of the major sources of uncertainty in future climate predictions (Boucher et al., 2013; Myhre et al., 2013; Mülmenstädt and Feingold, 2018). This arises partly from the wide range of scales involved in cloud systems,



where a knowledge of cloud micro-physics, particularly cloud-aerosol interaction, is critical to predict large scale phenomena
25 such as cloud radiative forcing or precipitation.

To address this and other related issues, the ACTRIS Aerosols, Cloud and Trace Gases Research Infrastructure is establishing an state of the art ground based observation network (Pappalardo, G., 2018). Within this organization, the Centre for Cloud Remote Sensing CCRES is in charge of creating and defining calibration and quality assurance protocols for the observation of Cloud properties across the complete network.

30 One of the key instruments for cloud remote sensing stations is the Cloud Radar. Cloud radars enable retrievals of several relevant parameters for cloud research, including but not limited to liquid water and ice content profiles, cloud boundaries, cloud fraction, precipitation rate and turbulence (Fox and Illingworth, 1997; Hogan et al., 2001; Wærsted et al., 2017; Dupont et al., 2018; Haynes et al., 2009). Additionally, recent studies revealed the potential of cloud radars to support a better understanding of fog processes (Dupont et al., 2012; Boers et al., 2013; Wærsted et al., 2019).

35 However, calibration remains a crucial factor in the reliability of radar retrieved data (Ewald et al., 2019). Systematic differences of 2 dB have already been observed, for example, between the satellite based radar CloudSat and the Lindenberg MIRA (Protat et al., 2009). This is a very important issue, since calibration errors as small as 1 dB would already introduce uncertainties in liquid water and ice content retrievals in the order of 15-20% (Fox and Illingworth, 1997; Ewald et al., 2019).

Since the objective of the CCRES is to guarantee a network of high quality observations, it is essential to develop standard-
40 ized and repeatable calibration methods for its instrumental network.

This paper presents an absolute calibration method for W band radars. It has been developed based on results from two experimental calibration campaigns performed at the SIRTAs Atmospheric Observatory, located in Palaiseau, France (Haefelin et al., 2005). The SIRTAs observatory hosts part of the ACTRIS CCRES infrastructure. For the experiments we used a BASTA-Mini W band Frequency Modulated Continuous Wave (FMCW) Radar, with scanning capabilities (Delanoë et al.,
45 2016). Nevertheless, the principles, procedures and limitations presented here should be applicable for any radar with similar characteristics, even when operating in another frequency band.

The method consists on an end-to-end calibration approach, consisting in retrieving the radar calibration coefficient by sampling the power reflected from a reference reflector mounted on top of a mast (Chandrasekar et al., 2014). A depth analysis of uncertainty and bias sources is performed, with the objective of reducing uncertainty under 0.5 dB. This low uncertainty in
50 the calibration would not only be useful for high quality retrievals, but also enables the use of the radar as a reliable reference for calibration transfer to other ground or space based cloud radars (Bergada et al., 2001; Protat et al., 2011; Ewald et al., 2019).

The article is structured as follows: Section 2 present the equations and theoretical considerations involved in the calibration exercise. Section 3 shows the experimental setup, complemented by section 4 where the experimental procedure and data treatment is presented. Section 5 presents an analysis of the sources of uncertainty and bias involved in our calibration experiment.
55 Section 6 presents the final calibration results, the uncertainty budget and an analysis of the variability in the calibration bias correction, followed by the conclusions.



2 Equations used in Radar Calibration

The absolute calibration of a radar consists in determining the calibration terms C_Γ and C_Z . They enable the calculation of Radar Cross Section Γ (RCS) or Radar Equivalent Reflectivity Z_e respectively, from the power backscattered by a punctual or distributed target towards the radar (Bringi and Chandrasekar, 2001).

Equation (1a) presents an expression for the RCS calibration term $C_\Gamma(T)$ of a FMCW radar, in dB , as a function of its internal parameters. The deduction of this expression is shown in the supplementary material. G_t and G_r are the maximum gain of the transmitting and receiving antennas respectively, dimensionless. λ is the wavelength of the carrier wave in meters and P_t is the power emitted by the radar in watts. The gain of solid state components changes with variations in their temperature T . Thus we make this dependence explicit in the receiver loss budget $L_r(T)$ and in the transmitter loss budget $L_t(T)$. The loss budget is the product of all losses divided by the gain terms at the end of the receiver or emitter chain, and has no dimensions.

In theory, $C_\Gamma(T)$ can be calculated by characterizing the gains and losses of every component inside the radar system and adding them. This can be very challenging, depending on the complexity of the radar hardware and the available radio frequency analysis equipment. In addition, with this procedure it is not possible to quantify losses due to interactions between different components, specially changes in antenna alignment or radome degradation (Anagnostou et al., 2001). This motivates the implementation of an end-to-end calibration, which consists on the characterization of the complete radar system at once by using a reference reflector and Eq. (1b).

$$C_\Gamma(T) = 10 \log_{10} \left(\frac{L_t(T)(4\pi)^3}{L_r(T)G_tG_r\lambda^2P_t} \right) \quad (1a)$$

$$= \Gamma - 2L_{at} - 40 \log_{10}(r_0) - P_r(r_0) \quad (1b)$$

Equation (1b) links the calibration term $C_\Gamma(T)$ to the RCS Γ of a target at a distance r_0 . Γ is usually expressed in $dBsm$ units (decibels referenced to a square meter), L_{at} is the atmospheric attenuation between the object and the radar in $dB km^{-1}$, which can be calculated using a millimeter-wave attenuation model (for ex. (Liebe, 1989)) and $P_r(r_0)$ is the power received from the target in unreferenced dB .

In Eq. (1a) we state that the calibration value has a temperature dependency. This T dependency of the gain is reflected in Eq. (1b) as variations in the value of $P_r(r_0)$. Experimental results indicate that $C_\Gamma(T)$ can be approximated by a linear relationship, shown in Eq. (2). Here n is the temperature dependency term in $dB \text{ } ^\circ C^{-1}$, T the internal radar temperature in $^\circ C$, T_0 a reference temperature value in $^\circ C$ and C_Γ^0 a term we name the *calibration coefficient*, in dB . More details about this approximation can be found in Sect. 5.4.

$$C_\Gamma(T) = C_\Gamma^0 + n(T - T_0) \quad (2)$$

Each $P_r(r_0)$ measurement is associated to a $C_\Gamma(T)$ value with Eq. (3b). Then, with the temperature dependency n known, we use Eq. (2) to compute a C_Γ^0 sample. After, n and C_Γ^0 are used to calculate $C_\Gamma(T)$ and then the radar Equivalent Reflectivity



calibration term $C_Z(T)$, in dB , with Eq. (3a) (Yau and Rogers, 1996). This relationship assumes the radar has two identical parallel antennas with a Gaussianly shaped main lobe. Θ is the antenna beamwidth in radians, δr is the radar distance resolution in meters and $|K| = |(\epsilon_r - 1)/(\epsilon_r + 2)|$ is a parameter related to the complex dielectric constant ϵ_r of the scattering particles (for weather radar usually liquid water or ice).

As with $C_\Gamma(T)$, $C_Z(T)$ enables the calculation of the Radar Equivalent Reflectivity term Z_e , in dBZ units, by using the relationship of Eq. (3b).

$$C_Z(T) = 10 \log_{10} \left(\frac{8 \ln(2) \lambda^4 10^{18}}{\theta^2 \pi^6 K^2 \delta r} \right) + C_\Gamma(T) \quad (3a)$$

$$= Z_e - 2L_{at} - 20 \log_{10}(r) - P_r(r) \quad (3b)$$

95 3 Experimental setup

Two calibration campaigns that lasted one month each were performed in May-June of 2018 and March-April of 2019 at the SIRTA observatory, located in Palaiseau, France (Haefelin et al., 2005). The observatory has a 500 meter long grass field in an area free of buildings, trees or other sources of clutter, well suited to install our calibration setup, shown in Fig. 1.

The instrument used for the calibration experiments is a BASTA-Mini. BASTA-Mini is a 95 GHz FMCW radar with scanning capabilities and two parallel Cassegrain antennas (Delanoë et al., 2016). The antennas are separated by 35 cm, and have a Fraunhofer far field distance of ≈ 50 m with a Gaussianly shaped main lobe (verified experimentally in Sect. 5.2). Transmitted power is fixed to 0.5 W, and is under constant monitoring using a diode with an uncertainty of ≈ 0.4 dB. The diode enable the monitoring of $L_t(T)$ variations, yet our experiments have shown that T is a better indicator to capture the variability of $C_\Gamma(T)$. This is likely because internal temperature changes affect both $L_r(T)$ and $L_t(T)$ simultaneously, and therefore the information provided by the diode is not sufficient to capture the behavior of the whole system. The results of the temperature dependency study for our radar is shown in Sect. 5.4).

This radar also includes hardware to enable the tuning of the carrier wave frequency within a range of ≈ 1 GHz, centered at 95 GHz. During the experiments we fixed the BASTA-Mini base frequency at 95.64 GHz to avoid any interference with the other two W band radars operating in parallel at the same site.

Our reference targets are two Triangular Trihedral Reflectors (also known as Corner Reflectors) composed by three orthogonal triangular conducting plates. Trihedral targets have a large RCS for their size and a low angular variability of RCS around their boresight (Atlas, 2002; Doerry and Brock, 2009; Chandrasekar et al., 2014). One reflector has a size parameter of 10 cm, with a maximum RCS at our radar operation frequency of 42.63 m². The other is 20 cm with a maximum RCS of 682.10 m² (Brooker, 2006). These targets were mounted on top of masts B and C in Fig. 1 respectively. Only mast C was used in the 2018 campaign, while both were used in 2019.

To align the system first we aim the radar towards the approximate position of the target. Second, we aim the target by slowly changing pan-tilt angles in the motor on mast B, or axially rotating the tube of mast C to maximize power measured at the



Figure 1. Experimental setup for 2018 and 2019 calibration experiments: (A) Scanning BASTA-Mini radar located in a reinforced platform 5 m above the ground. (B) 10 m mast with a 10 cm triangular trihedral target mounted on a pan-tilt motor with an angular resolution and repeatability better than 0.1° . This mast has microwave absorbing material wrapped to it to reduce its RCS (clutter). The 10 m mast was only installed in the 2019 calibration campaign. (C) 20 m mast with a 20 cm triangular trihedral target. The target aiming is fixed relative to the mast. This mast is used in both 2018 and 2019 calibration campaigns. Angular separation between the masts is enough to sample both targets without mutual interference.



radar's end. Third, radar aiming is tuned around target position until the maximum reflected power is found. Finally, we repeat the second step, after which we have the system ready to sample $P_r(r_0)$.

120 It must be mentioned that this procedure does not guarantee a perfect alignment. In fact, it is impossible to have every element perfectly adjusted because of limits in the positioner resolution or uncertainties introduced when installing each element. Sections 4 and 5.5 explain how we deal with these limitations.

4 Methodology

This section describes the procedure followed when performing calibration experiments using the setup described in Sect. 3. 125 The methodology has the objective of quantifying and correcting when possible all sources of uncertainty to enable a reliable estimation of the calibration terms $C_\Gamma(T)$ and $C_Z(T)$.

A challenge we found when using targets mounted on masts to estimate C_Γ is that the value of Γ may vary depending on how components are aligned. Our studies have shown that for the feasible alignment accuracy we can get when installing our setup, this effect is in the order of tenths of dB , and therefore not negligible. Additionally, we concluded that if we left this 130 uncertainty source uncorrected, we would introduce a bias in the calibration result (see Sect. 5.5).

The flow chart of Fig. 2 illustrates the calibration procedure. To quantify the bias introduced by alignment uncertainty we decided to divide each calibration experiment in N iterations. Each iteration consists on a system realignment, followed by sampling of the target signal $P_r(r_0)$ for one hour.

The period chosen to perform the sampling is important, because it will have an incidence on how stable is the calibration 135 value. To minimize uncertainty it is recommended to perform calibration iterations when the atmosphere is clear, there is no rain and wind speed is under 1 ms^{-1} . However, these requirements may change depending on how robust is each setup to atmospheric conditions.

FMCW radars have a discrete distance resolution. Consequently, power measurements vs distance will be resolved in finite discrete points, usually named gates. Because of this resolution limitation, power received from a point target is split between 140 the gates closer to its position (Doviak and Zrnić, 2006). To correctly assess the total reflected power we set the radar resolution to 12.5 meters (chirp bandwidth of 12 MHz), and its integration time to 0.5 seconds. This resolution is high enough to accurately identify the peak of power coming from the target while avoiding the introduction of additional clutter from the trees located further.

To calculate $P_r(r_0)$ we add five gates: the target's gate plus two before and two after the target's position. Adding more 145 contiguous gates increase the power value by less than 0.01 dB , thus we conclude that these five gates concentrate almost all the power reflected back from the target.

Then $P_r(r_0)$ is corrected considering compression effects and antenna overlap losses (Sects. 5.1 and 5.2). For each corrected $P_r(r_0)$ sample we proceed to calculate a single C_Γ value. Atmospheric attenuation L_{at} is calculated using in-situ atmospheric observations and the model published by Liebe (1989).

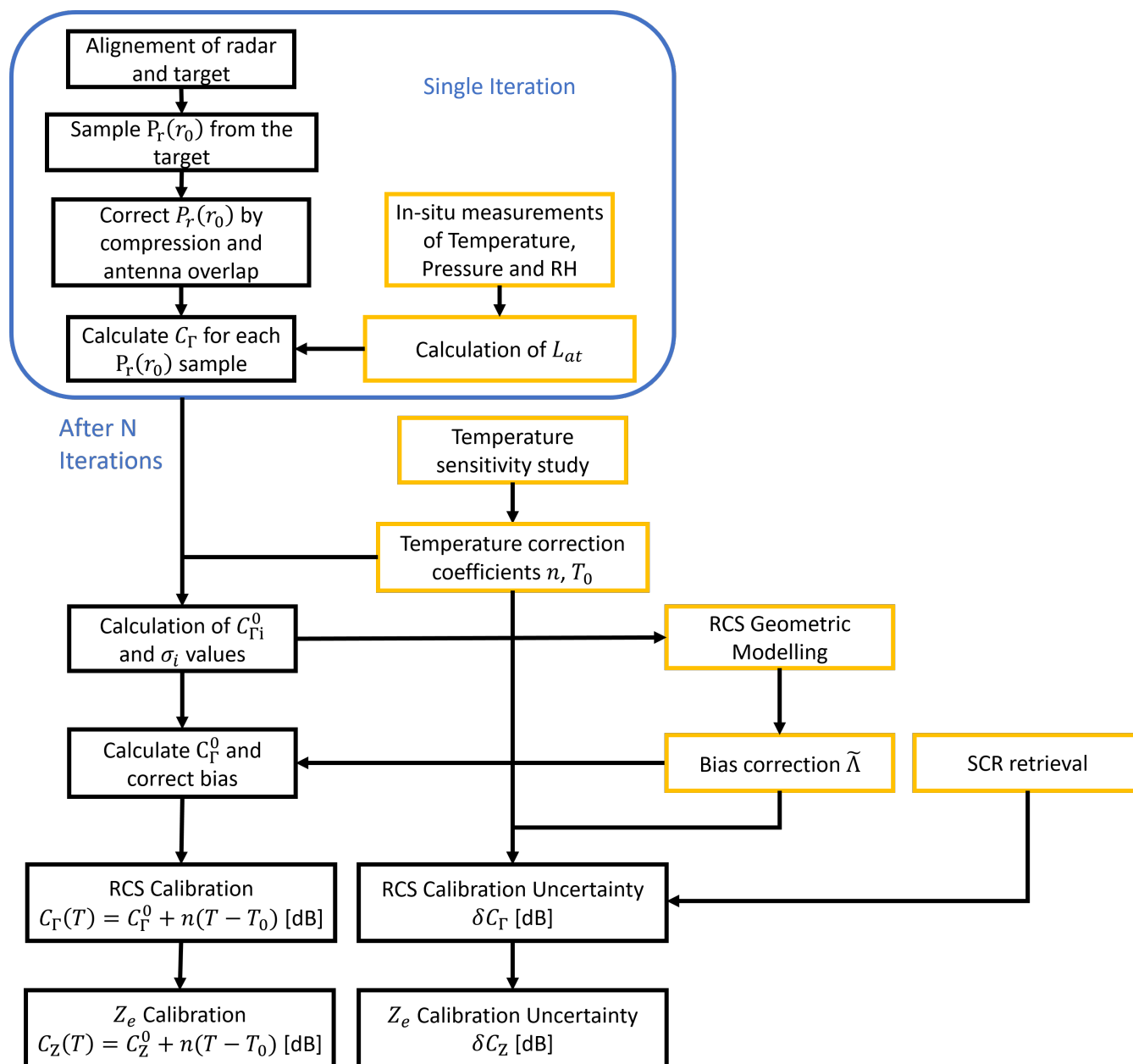


Figure 2. Summary of a complete calibration process. Each calibration requires repetition of system realignment and sampling steps, called iterations. During each iteration we continuously sample the power reflected from the reference target position for one hour (power corrections in Sect. 5.1). The retrieval of N iterations enable the estimation of the system bias due to misalignments in the setup (Sect. 5.5). Temperature dependency is retrieved in an independent experiment (Sect. 5.4). Uncertainty introduced by clutter signals at the target location is also included in the total uncertainty budget (Sect. 5.3).



150 We performed one calibration experiment with 6 iterations during the 2018 campaign using the 20 m mast. In the 2019 campaign we did two experiments: one with 10 iterations using the 10 m mast and another with 2 iterations on the 20 m mast (Fig. 1). During these campaigns we also retrieved the temperature dependency coefficients n and T_0 experimentally (see Sect. 5.4). Temperature dependency coefficients enable the calculation of a C_Γ^0 value for each sampled C_Γ .

From each iteration we get a distribution of resulting C_Γ^0 values with a small spread introduced by second order effects. The average value of each iteration i is named $C_{\Gamma i}^0$, and its corresponding standard deviation is named σ_i . With this information we proceed to calculate the bias corrected calibration coefficient C_Γ^0 , by using Eq. (4). $\tilde{\Lambda}$ is the bias correction term.

$$C_\Gamma^0 = \frac{1}{N} \sum_{i=1}^N C_{\Gamma i}^0 - \tilde{\Lambda} \quad (4)$$

Equation (5) shows the uncertainty budget linked to the aforementioned estimator of C_Γ^0 . δC_Γ and δC_Z are the resulting uncertainties of $C_\Gamma(T)$ and $C_Z(T)$ respectively. The terms σ_T^2/N and $\sum \sigma_i^2$ come from propagating the uncertainty when averaging the $C_{\Gamma i}^0$ terms. σ_Λ the uncertainty of the bias correction and σ_{SCR} is the uncertainty introduced by clutter. Clutter is the presence of unwanted echoes which affect our reading of $P_r(r_0)$, coming from reflections on other objects in the environment. The method to quantify the uncertainty σ_{SCR} uses a parameter named Signal to Clutter Ratio (SCR), explained in detail in Sect. 5.3. Finally, the additional σ_T term appears when calculating $C_\Gamma(T)$ or $C_Z(T)$ with Eq. (2) during the radar operation.

$$\delta C_\Gamma = \sqrt{\frac{1}{N^2} \sum_{i=1}^N \sigma_i^2 + \frac{\sigma_T^2}{N} + \sigma_T^2 + \sigma_{SCR}^2 + \sigma_\Lambda^2}$$

$$165 \quad \delta C_Z = \delta C_\Gamma \quad (5)$$

We additionally observe that RCS and Z_e calibration uncertainty is the same. This comes from the following observations: Wavelength variations coming from the chirp and distance resolution uncertainties contribute less than 0.01 dB to the uncertainty budget. Uncertainty introduced by assuming a Gaussian beam shape is neglected, because the RMSE between the Gaussian fit and the manufacturer's characterization of the antennas is less than 0.01 dB within the HPFW region (see Sect. 5.2).

It is worth noting that ϵ for water at the W band can vary significantly with temperature. Using the results published by Meissner and Wentz (2004), we calculate that $|K|$ varies from ≈ 0.83 to ≈ 0.92 between -5 and 25 °C. This variability translates as a change of -0.5 to $+0.5$ dB in C_Z , respectively. For this study we'll use the reference value $|K| = 0.86$, corresponding to pure water at 5 °C, however if lower uncertainty in Z_e retrievals is necessary this value should be corrected by using in-situ or remote sensing retrievals of cloud temperature. The same applies to the estimation of L_{at} . Thus, uncertainty in the calibration is not the same as the uncertainty in the retrievals but rather its lower bound.



5 Sources of uncertainty and bias in Absolute Calibration with corner reflectors

In this section we identify and quantify the uncertainty and bias introduced by several terms in Eq. (1b). Following the recommendations in the work of Chandrasekar et al. (2014), we considered the impact of receiver saturation, signal to clutter ratio, antenna lobe shape and overlap, and environmental conditions. Additionally, we considered the impact of temperature fluctuations inside the radar box and of imperfect alignment of the reference target.

5.1 Receiver compression

It is advisable to design calibration experiments which avoid the appearance of compression effects. If this is not possible, compression must be considered in the data treatment so that the retrieved calibration remains valid in the receiver's linear regime, where it usually operates during cloud sampling (Scolnik, 2000).

For studying how these effects could affect our calibration, we retrieved the radar's receiver power transfer curve. Receiver characterization was done by removing the radar's antennas and connecting the emitter's end to the receiver's input, with two attenuators in between. The first was a 40 dB fixed attenuator, while the second was a tunable attenuator covering the range between 50 and 1 dB of losses. The adjustable attenuator enabled the retrieval of the power transfer curve by varying the attenuation and sampling the power at the receiver's end (digital processing included). Our retrieved power transfer curve is shown in Fig. 3 (a).

Compression effects must be considered in calibration, or a bias will be introduced. In consequence, we include compression correction in every sample of reflected power, which consists on projecting their value to the ideal linear response using the power transfer curve.

For example, the power received from the 20 cm target on the 20 m mast returned was 198.7 dB in average, before corrections. The power transfer curve shows that at this power values we have a loss caused by compression of ≈ 0.3 dB. After correcting each power sample by compression with the power transfer curve, we obtain a corrected power average value of 199.1 dB. On the other hand, for the 10 cm target on the 10 m mast the average power value before corrections is 197.8. Because this value is lower than what is obtained the 20 m mast, the associated compression effect is also smaller, of ≈ 0.2 dB. After applying this correction to each power sample we end with a new corrected power average of 198.0 dB.

5.2 Antenna Properties

We took advantage of our experimental setup and the scanning capabilities of the radar to check if the radar antennas were properly aligned and if their beam width matched the specifications provided by the manufacturer. This was done by using the target on the 20 m mast. Results are shown in Fig. 3 (b).

Manufacturer specifications indicate that antenna beamwidth should be of 0.8° . However, data from an experimental characterization done by the same manufacturer in an anechoic chamber indicate that antenna beam shape is better approximated by a Gaussian with a Half Power Beam Width (HPBW) of $\theta \approx 0.88^\circ$. The total gain difference between the experimental curve and the Gaussian approximation of ≈ 0.0003 dB in the HPBW region.

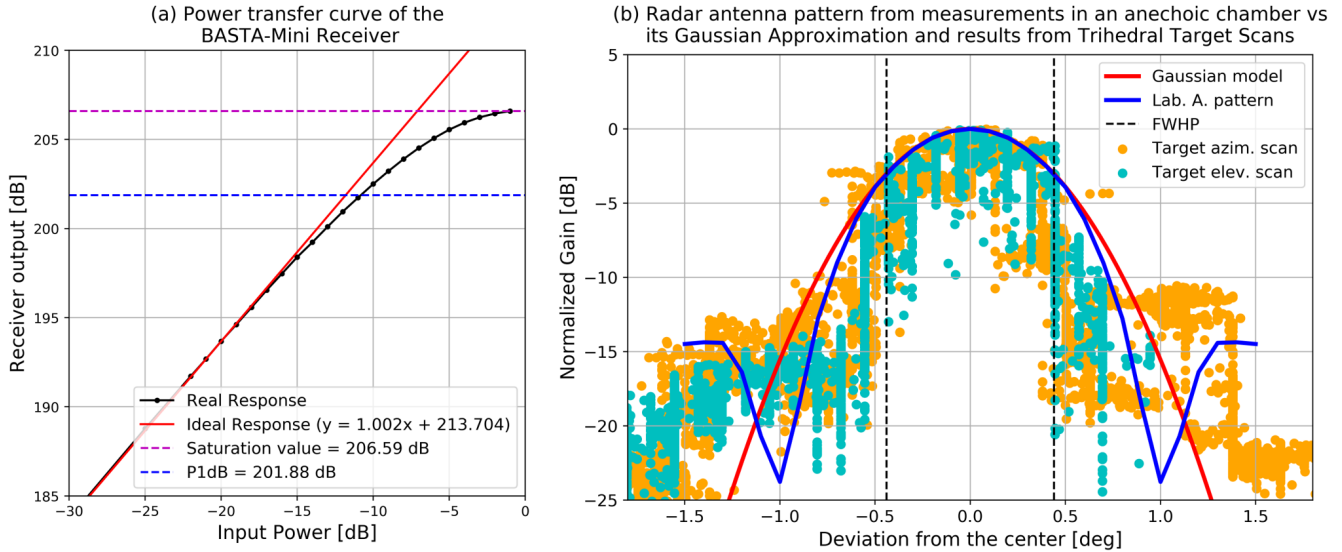


Figure 3. (a) Power transfer curve of the BASTA-Mini receiver. All our signal retrievals from the target are slightly under 200 [dB] line, thus the correction required due to compression effects is small (< 0.3 dB). (b) Normalized antenna pattern of the BASTA-Mini antennas. We can observe that the Gaussian fit is very close to the antenna gain curve measured at the manufacturer’s laboratories and the results from our scans, specially within the HPBW area (3 dB loss). This fit has a beamwidth of $\theta = 0.88^\circ$.

The beamwidth of 0.88° is consistent with what we observe in our scanning results. This indicates that we can assume the antennas to be parallel, allowing the introduction of a correction for losses caused by incomplete antenna overlap. The correction, shown in Eq. (6), accounts for the loss of power that would be received from a point target compared to a monostatic system (Sekelsky and Clothiaux, 2002). This loss occurs because a point target cannot be in the center of two non-concentric parallel antenna beams.

$$L_o = \exp\left(\frac{2 \arctan\left(\frac{d}{2R}\right)^2}{0.3606 \theta^2}\right) \quad (6)$$

Equation (6) assumes that the radar has two identical, parallel antennas with gaussian beam shape. Their main axis is separated by a distance d , and the point target is located at a distance R , facing the geometrical center of the radar, where the gain is maximum. For the BASTA-Mini $d = 35$ cm. This introduces a loss of 0.08 dB for the target at 196 meters of distance, and of 0.02 dB for the target at 376.5 meters.

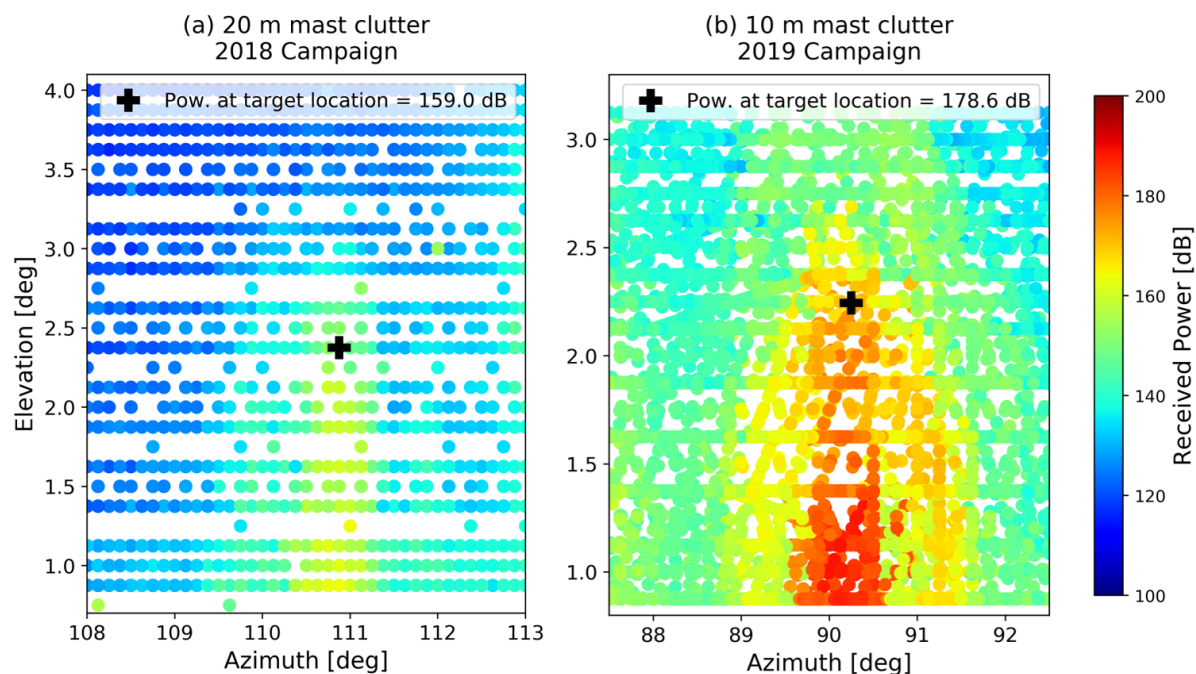


Figure 4. Clutter retrieval from the 10 m (a) and 20 m mast (b) respectively. Masts are scanned without the reflectors to measure the clutter signal. The nominal target position is marked with a black cross.

5.3 Signal to Clutter Ratio

220 The power sampled from our reference reflector is an addition of the power from the target (signal) and unwanted reflections
on other elements in the environment, such as the ground or the mast (clutter). We observed that this clutter dominates above
the radar noise, and thus becomes the main source of interference in our calibration signal.

To quantify the impact of clutter we use the Signal to Clutter Ratio (SCR) parameter. It is calculated as the ratio of total
power received from the target to power received from clutter under the same configuration, but with the reference reflector
225 removed. SCR enables the uncertainty σ_{SCR} introduced by clutter in the sampled $P_r(r_0)$ values to be computed (Chandrasekar
et al., 2014).

Clutter power is sampled and corrected with the same corrections used in $P_r(r_0)$ retrievals, but in a scanning pattern mode
to capture clutter around the whole target area. Figure 4 shows our results from scanning around the 10 and 20 m masts with
targets removed.

230 We observe that the 10 m mast is more reflective than the 20 m one. This may be caused by its smaller height (more ground
clutter) and its larger geometrical cross-section. We can also see that the signal in the 10 m is stronger where absorbing material
is not present (below $\approx 1.5^\circ$ of elevation). In both cases we didn't detect any signal from the nearby trees close to the target's
position.



To calculate SCR we compare the average power received from each target during the calibration experiments with the
235 maximum clutter power observed in a region of 0.125° around the target's coordinates, vertically and horizontally. The value
is taken from the radar's positioner resolution.

The average reflected power from 10 cm target on the 10 m mast is 198.0 dB. This provides an SCR value of 19.4 dB, which
implies a σ_{SCR} uncertainty value of ≈ 0.93 dB. From the 20 cm target on the 20 m mast, the average reflected power is 199.1
dB. Its SCR equals 40.1 dB, which is translated as an uncertainty contribution of $\sigma_{SCR} \approx 0.09$ dB. From the results we see
240 that even if target alignment is better with the 10 m mast, calibration results may not get less uncertain because the motor used
for target alignment acts as a big source of clutter.

5.4 Temperature correction

BASTA-Mini has a regulation system to control temperature fluctuations inside the radar box. However, since the radar is based
on solid state components, even small temperature fluctuations may impact the performance of the transmitter and receiver, and
245 therefore affect the calibration stability. To account for this effect we introduced a temperature dependency in the calibration
term, shown in Eq. (2).

During the experiments we verified the need of this correction by observing that the retrieved calibration term $C_T(T)$ has
a consistent change depending on the time of the day, and that this change is strongly correlated to the temperature inside the
radar.

250 Figure 5 (a), (b) and (c) show the results of a representative experiment done in the 2018 campaign. Here we left the radar
sampling the target signal for several hours, to observe the variability of $C_T(T)$ during the day. (a) shows the raw result in
the RCS calibration term $C_T(T)$. There is a spread of almost 1 dB between the maximum and minimum values during the
whole timeseries. (b) is a fourier transform of this raw timeseries. Here we can see that most of the variability happens in
the timescale of hours. (c) presents the timeseries of (a), but in a daily cycle perspective. Here we plot hourly means of the
255 deviation of $C_T(T)$ with respect to the total average, with its hourly standard deviation as errorbars. We also superimposed
atmospheric attenuation and the radar amplifier temperature to show that the first has a much smaller impact in calibration
variability compared to the second.

To retrieve the temperature dependency we use a linear regression over all the experiments done in 2018 and 2019, shown in
Fig. 5 (d). In this case the data used was not limited to one hour, to maximize the range of temperatures covered. The regression
260 shows that the variability in the calibration term has an almost linear relationship with internal radar temperature, in the dB
scale, and it is the same for both campaigns.

The analysis enable us to obtain estimations for the terms of the temperature dependency part of Eq. (2). We obtain the
value $n = 0.093$ dB $^\circ C^{-1}$, with $T_0 = 26.5$ $^\circ C$. This reference T_0 is chosen because it is approximately the average internal
temperature when considering all the experiments.

265 When calculating the RMSE between the linear regression and all data, we get the value $\sigma_T = 0.13$ dB. This remaining
error may be introduced by the combination of random noise and other non identified second order sources, so we included it
in the final uncertainty budget of the calibration.

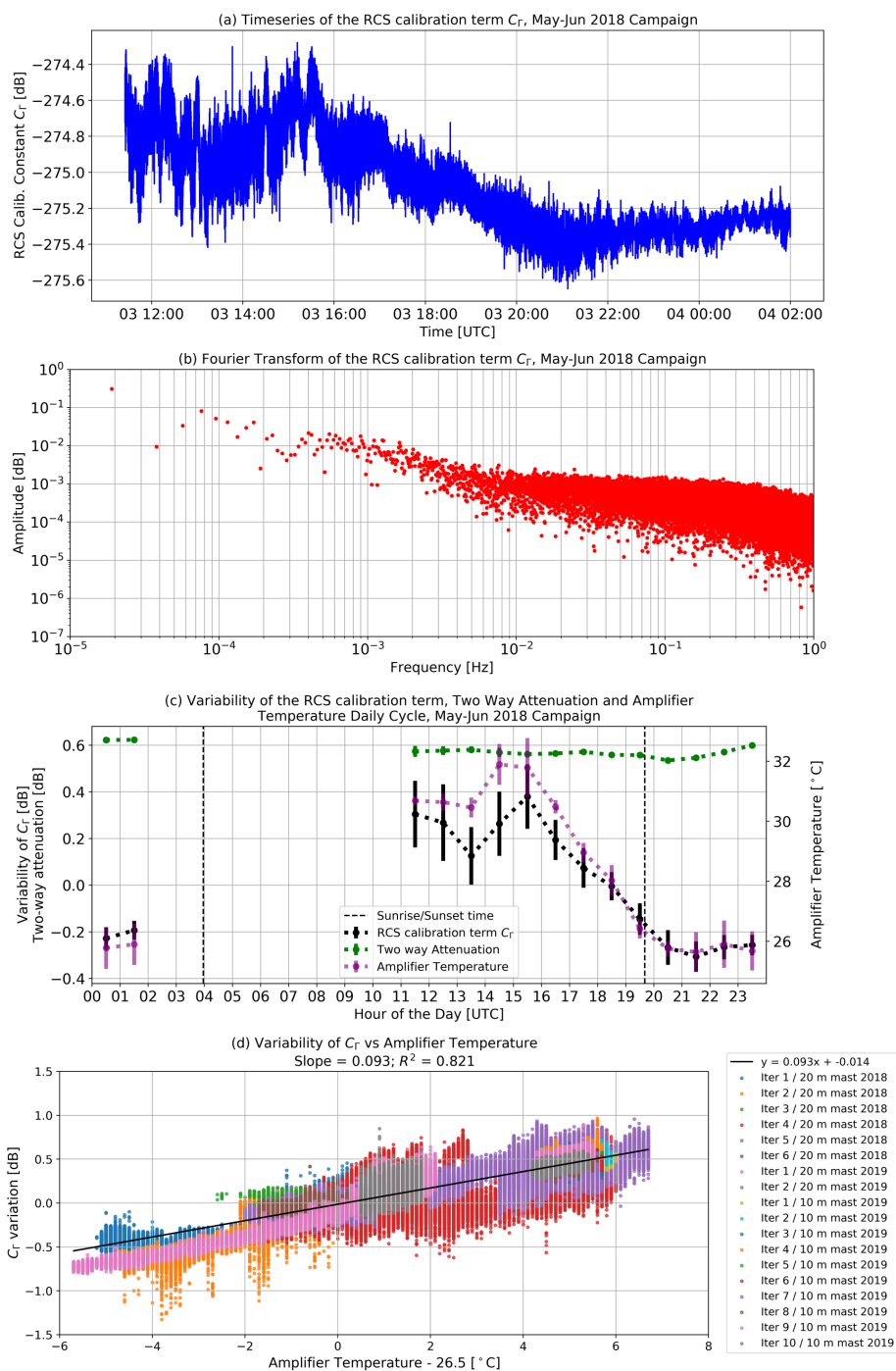


Figure 5. Study of calibration variability. Samples from iteration 5, 2018 Calibration Campaign. (a) Time series of the RCS Calibration term retrieval. (b) Fourier transform of the RCS Calibration term after subtracting the mean value. (c) Daily Cycle of calibration variability, amplifier temperature and two-way attenuation. Attenuation errorbars are too small to be seen with this scale. (d) Regression of the relative changes in the $C_r(T)$ versus amplifier temperature, calculated using all samples from 2018 and 2019 campaigns.



5.5 Misalignment Bias

The retrieval of $C_{\Gamma}(T)$ using Eq. (1b) requires a precise knowledge of the reference target effective RCS Γ_0 . Each $dBsm$ of
270 difference between the theoretical value used in calculations and the effective target RCS will introduce a bias of the same
magnitude in the estimation of the calibration coefficients C_{Γ}^0 , and thus in $C_{\Gamma}(T)$.

The effective reflector RCS is the actual physical value that would be measured by a perfectly calibrated radar. It is different
from the target intrinsic RCS which only depends on its physical properties. Effective RCS changes when the experimental
setup is modified. For example, if the point target is not exactly in the beam center, antenna gain won't be maximum and
275 therefore the effective RCS will decrease compared to the intrinsic value. Effective RCS also changes when the incidence
angle of the radar beam is modified. This latter effect may increase or decrease effective RCS depending on the original
situation.

A common approach in these type of experiments is to set Γ_0 to be the maximum theoretical RCS of the target, assuming
misalignment will cause a negligible deviation from this value. This procedure can be refined for cases where the system default
280 configuration does not have the target boresight aligned with the radar position. In these cases, effective RCS can be calculated
using equations derived from geometrical optics (more complex optical calculations may be necessary for other wavelengths
or target sizes). For example, we use the equations published by Doerry and Brock (2009) when calculating the effective RCS
of our Triangular Trihedral target on the 20 m mast.

Unfortunately, this approach does not correct the impact of alignment uncertainties. We observed that random errors in the
285 element positioning will statistically impact the effective Γ_0 in a single direction. Thus, simply taking the average of many
target sampling iterations would result in a biased estimation of the calibration.

With the objective of quantifying the impact of alignment uncertainties we developed a geometrical simulator of effective
RCS. This simulator receives as input the position of each element in the setup and calculates the effective RCS considering
the beam incidence angle and antenna gain variations when the target is not in the center of the beam. The degrees of freedom
290 included in the simulator are shown in Fig. 6 (a). It enables the modification of the radar aiming angles, the mast dimensions and
the positioning and orientation of the target. The equations used in the simulator can be found in the article support material.

We now use the simulator to study how uncertainty in alignment can affect the value of Γ_0 . For this, we model an example
experiment based on the 20 m mast setup. In this model we separate input variables between known and uncertain. Known
terms can be fixed or measured very precisely in the field experiment, hence they are set as fixed values. Meanwhile, uncertain
295 terms represent the parameters that cannot be fixed or measured very precisely, and for that reason are better expressed as
probability distributions (terms defined in Fig. 6 (a)).

– Known terms:

– $x_r = 376.5$ m

– $h_r = 5.3$ m

300 – $\rho = 20$ m



- $\alpha = 48^\circ$
- Target Size = 20 cm
- Variables with uncertainty:

- $\theta_r = \mathcal{N}(\theta_r^*, \sigma_{\theta_r}^2)$
- 305 - $\phi_r = \mathcal{N}(\phi_r^*, \sigma_{\phi_r}^2)$
- $\theta = \mathcal{N}(0, \sigma_\theta^2)$
- $\phi = \mathcal{U}([0^\circ, 360^\circ])$
- $\tau = \mathcal{N}(\tau^*, \sigma_\tau^2)$

In the uncertain variables, $\theta_r^* = 87.82^\circ$, $\phi_r^* = 0^\circ$ and $\tau^* = 0^\circ$ represent the nominal alignment angles, which are the values
310 expected under an ideal field experiment where the radar aims directly to the target and the mast is perfectly vertical. To these
nominal values we associate a distribution shape and the uncertainty set $\sigma_{\theta_r} = 0.075^\circ$, $\sigma_{\phi_r} = 0.075^\circ$, $\sigma_\theta = 1.5^\circ$, $\sigma_\tau = 5^\circ$. Each
term, known and uncertain, is estimated from observations done during the experimental field work.

With these input parameters we sample the Γ_0 distribution that would arise after a large amount of experimental iterations.
Figure 6 (b) shows the results from this sampling. The black dashed line shows the effective RCS under our experimental
315 configuration, when each element is in its nominal position. We can see that this effect cannot be neglected in our case, since
its value is 0.8 dB lower than the maximum theoretical RCS.

However, this single correction does not suffice. The results of the model show that the addition of uncertainty into the
process induces another bias of ≈ 0.3 dB, in average. Since this is within the order of magnitude of our desired uncertainty
in the calibration, the example clearly illustrates the need of including a bias correction step in our calibration methodology.

320 The details about how this correction is made are fully explained in the support material. Summarizing, the procedure relies
on using the standard deviation σ_ϵ between N experimental retrievals of C_Γ^0 as an indicator of the RCS distribution's shape.
Then, we simulate an space of possible uncertainty sets, based on our experimental configuration, to generate the distribution
 Λ . Λ indicates how likely is a given bias value when the spread between N experiments is σ_ϵ (with a tolerance of 5%). The
distribution Λ , shown in support material, is monomodal and asymmetric. Because of this we use its median $\tilde{\Lambda}$ as the best bias
325 correction estimator. In turn, the RMSE between Λ and $\tilde{\Lambda}$ is used to estimate the uncertainty σ_Λ of the bias correction, term
which is later added to the uncertainty budget.

6 Results

In 2018 we used the 20 m mast only, performing six iterations. For 2019 we did 10 iterations using the 10 m mast and 2
iterations with the 20 m mast. The distributions of C_Γ^0 obtained in each iteration and experiment is shown in Fig. 7.

330 The radar hardware changed between 2018 and 2019 campaigns due to experiments required to retrieve the power transfer
curve and perform maintenance operations. This implies that we cannot compare absolute calibration values between both
campaigns. What remains valid is to compare properties such as the variability, and the results from both experiments of 2019.

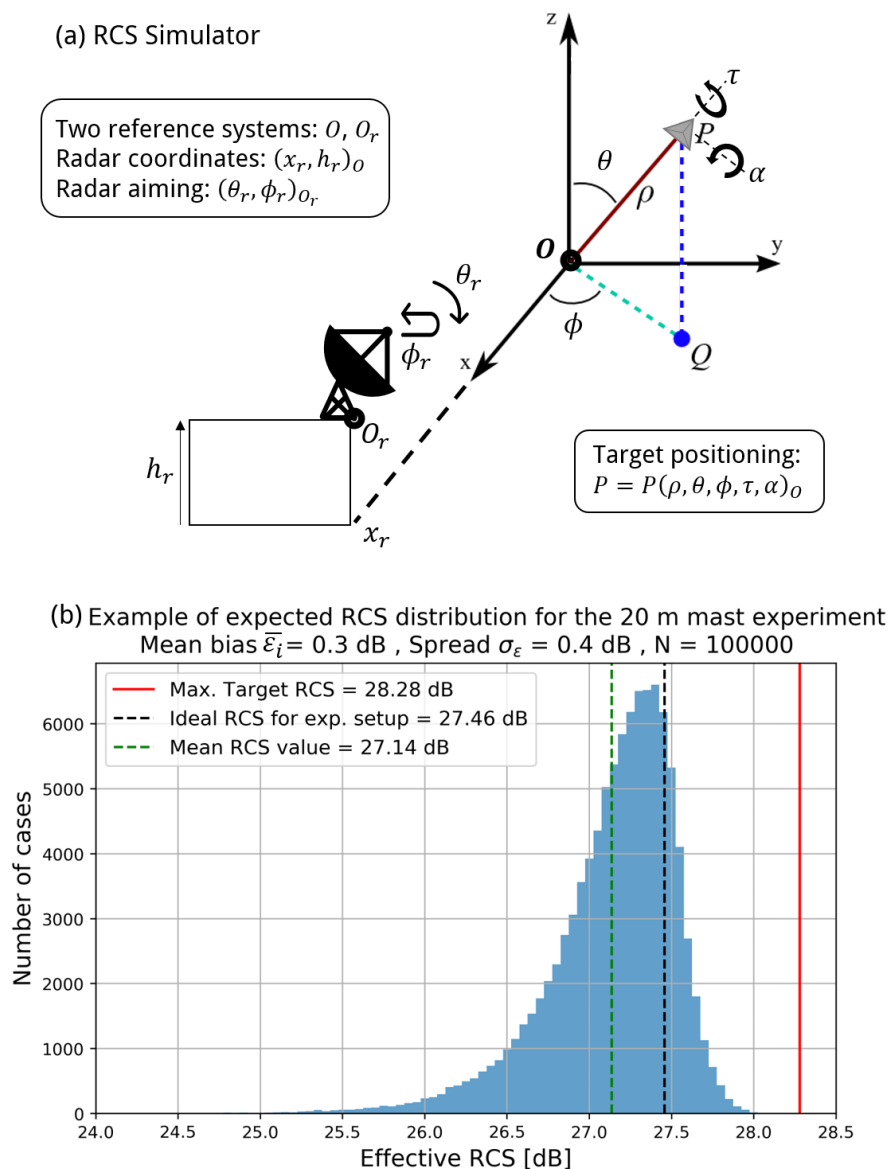


Figure 6. (a) Diagram of the RCS simulator illustrating its degrees of freedom. (b) Example of effective RCS distribution obtained after 100 000 simulations with the uncertainty set specified in the text. The simulations are based on our 20 m mast setup. Bias is calculated subtracting the ideal RCS by the mean RCS value. The example illustrates how the effective RCS will be, statistically, lower than the result expected from an ideally aligned setup.



In the results we can notice a difference in $C_{\Gamma_i}^0$ spread when comparing the 10 and 20 m masts. The 6 iterations of 2018 (Fig. 7 (A)) have an spread of $\sigma_\epsilon = 0.33$ dB, while the spread of the 10 iterations of 2019 is 0.11 dB (Fig. 7 (B)). This happens because the 10 m mast has a motor on top which enables a much finer adjustment of the target position, improving the repeatability of the experiments.

There is also a small difference in the spread of the curves. The $C_{\Gamma_i}^0$ values retrieved in experiment (B) have a smaller spread σ_i . This is because we took all the samples during one single night, with very clear conditions and an average wind speed below 1 m/s. A great advantage was the presence of the motor that enables target alignment in ≈ 5 minutes. Meanwhile, for experiment (A) curves were sampled during different days, because the 20 m mast setup requires more time to align (≈ 2 hours). The different conditions in each day led to a more varied shape in the retrieved curves. This effect is specially noticeable in experiment (C), where the iterations were performed during daytime, when atmospheric conditions are more dynamic, specially wind speed variability. The introduced variability was not fully compensated by our corrections and thus bimodal distributions remained. However, individual spread is still small, within ≈ 0.1 dB, so we decided to accept these samples for calibration purposes.

To study the dependency of the bias correction on the amount of iterations we calculate the bias correction term $\tilde{\Lambda}$ and its uncertainty σ_Λ of experiments (A) and (B) with different amounts of repetitions. The order of the iterations used in each row match the sequential order indicated in Fig. 7. The results are shown in Table 1. For both cases we have the best estimate when we use all the samples available for each experiment, and thus we use this bias correction and uncertainty when computing the calibration coefficient.

For experiment (C) we followed a different approach. Because we only have two samples, the calculated $\sigma_\epsilon = 0.2$ dB is very likely to be underestimated. Consequently, and because the experimental procedure was identical to what was done in 2018, we assume our parameters σ_ϵ , $\tilde{\Lambda}$ and σ_Λ to be equal to the best estimation of experiment (A). This is possible because in our methodology we assume that the bias probability distribution of a given system is unique, even if it is unknown, and what is done by performing many iterations is to successively restrict the possible sets of uncertainties that can generate results consistent with the observations. This latter hypothesis is consistent with the decrease in bias estimation uncertainty when increasing the amount of iterations.

Table 2 contains a summary of all corrections and uncertainty contributions involved in the calculation of the calibration, as introduced in Sect. 4. With the aforementioned results, we use Eqs. (4) and (5) to calculate to calculate the RCS and Reflectivity calibration terms $C_\Gamma(T)$ and $C_Z(T)$, alongside their uncertainty. $C_Z(T)$ is calculated for the range resolution $\delta r = 12.5$ m, which is the same mode used for target sampling. T is the radar amplifier temperature in $^\circ C$. Results are shown below.

– (A) 20 m mast - 2018:

$$\diamond C_\Gamma(T) = -275.6 + 0.093(T - 26.5) \pm 0.3 \text{ dB}$$

$$\diamond C_Z(T) = -191.5 + 0.093(T - 26.5) \pm 0.3 \text{ dB}$$

365 – (B) 10 m mast - 2019:

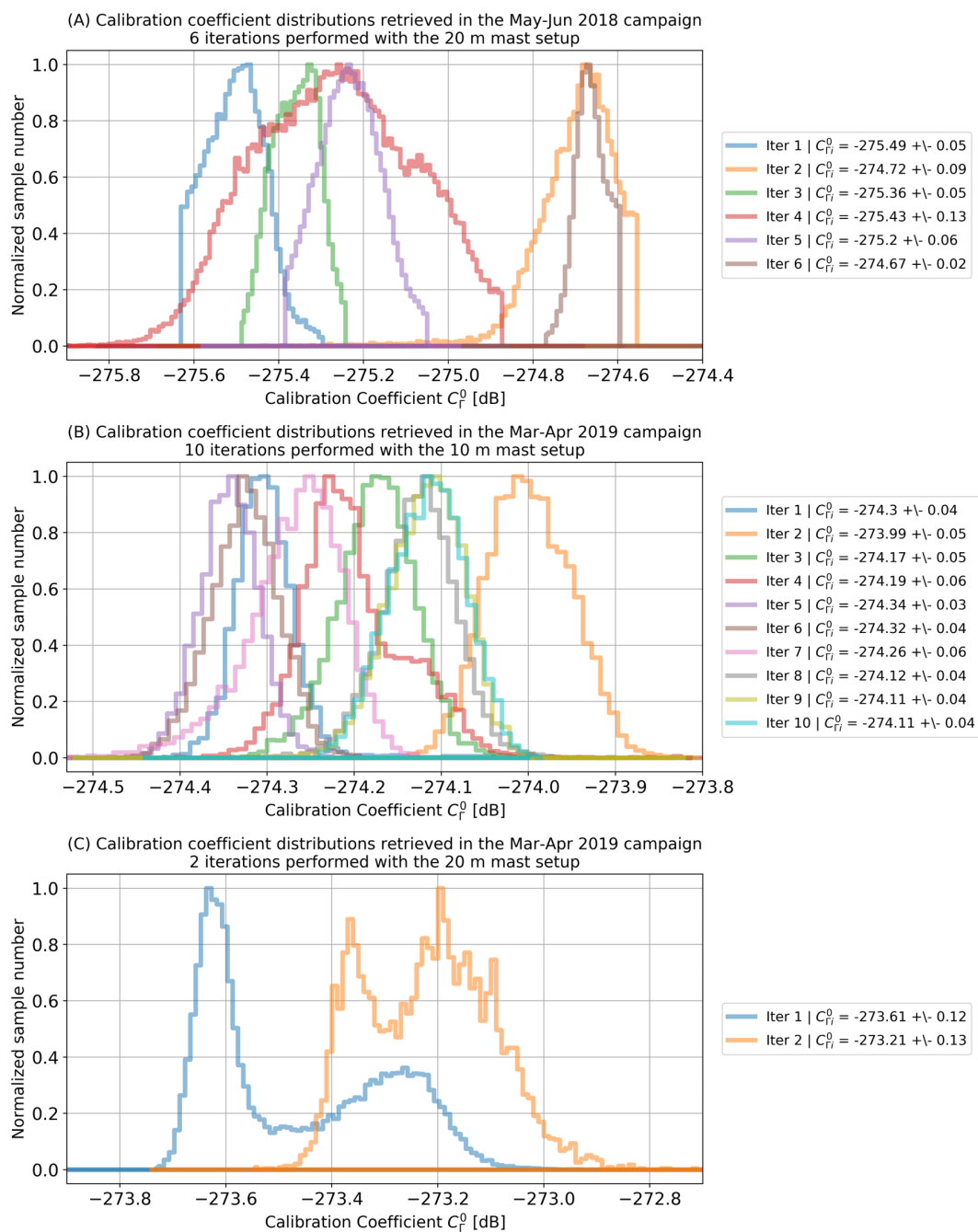


Figure 7. Calibration coefficient distributions obtained for (A) 2018 campaign using the 20 cm target on the 20 m mast, (B) 2019 campaign using the 10 cm target on the 10 m mast and (C) 2019 campaign with the 20 cm target on the 20 m mast.



Table 1. Bias correction $\tilde{\Lambda}$ and its uncertainty σ_{Λ} calculated using a different amount of iterations, for the experiments of 2018 and 2019 calibration campaigns (for ex. 3 iterations means we used iterations 1, 2 and 3 of the experiment). We include the average and spread σ_{ϵ} between the retrieved $C_{\Gamma_i}^0$ for each case. The estimation of $\tilde{\Lambda}$ and σ_{Λ} depends on the amount of iterations N and their associated σ_{ϵ} value.

(A) 20 m mast 2018 N° of iterations	Exp. Results		Bias Correction	
	$\frac{1}{N} \sum C_{\Gamma_i}^0$	σ_{ϵ} [dB]	$\tilde{\Lambda}$ [dB]	σ_{Λ} [dB]
2	-275.11	0.38	0.98	1.78
3	-275.19	0.33	0.65	0.86
4	-275.25	0.31	0.51	0.50
5	-275.24	0.28	0.40	0.33
6	-275.14	0.33	0.44	0.28
(B) 10 m mast 2019				
N° of iterations				
2	-274.15	0.15	0.78	1.65
3	-274.15	0.12	0.42	0.70
4	-274.16	0.11	0.27	0.34
5	-274.20	0.12	0.24	0.20
6	-274.22	0.12	0.22	0.13
7	-274.23	0.11	0.19	0.10
8	-274.21	0.11	0.18	0.07
9	-274.20	0.11	0.17	0.06
10	-274.19	0.11	0.16	0.05
(C) 20 m mast 2019				
N° of iterations				
2	-273.41	-	0.44	0.28

$$\diamond C_{\Gamma}(T) = -274.4 + 0.093(T - 26.5) \pm 0.9 \text{ dB}$$

$$\diamond C_Z(T) = -190.3 + 0.093(T - 26.5) \pm 0.9 \text{ dB}$$

– (C) 20 m mast - 2019:

$$\diamond C_{\Gamma}(T) = -273.9 + 0.093(T - 26.5) \pm 0.4 \text{ dB}$$

$$\diamond C_Z(T) = -189.8 + 0.093(T - 26.5) \pm 0.4 \text{ dB}$$

370

Finally, we performed a test of the calibration by measuring a altostratus cloud in both campaigns (Fig. 8). The sampling was done with the 25 m resolution, and thus 6 dB had to be subtracted from the $C_Z(T)$ calibration calculated for the 12.5 m resolution. In this correction, 3 dB come from the change in the distance resolution term δr (Eq. (3a)), and the other 3 dB are subtracted to compensate the additional digital gain coming from doubling the amount of points in the chirp fourier transform



Table 2. Summary of all corrections and uncertainty contributions in the calculation of $C_{\Gamma}(T)$. The absolute correction terms have a sign associated to the direction in which they impact the final calibration calculation. For the compression correction we present the average magnitude and for the temperature correction we present the range of possible values.

Absolute Corrections	Term [dB]	(A) 20 m mast 2018	(B) 10 m mast 2019	(C) 20 m mast 2019
Compression	Fig. 3 (a)	-0.3 in avg.	-0.2 in avg.	-0.3 in avg.
Partial Antenna Overlap	L_o	-0.02	-0.08	-0.02
Temp. Corr. ($T_0 = 26.5$ °C)	$n(T - T_0)$	within ± 0.6	within ± 0.6	within ± 0.6
Misalignment Bias	$\tilde{\Lambda}$	-0.44	-0.16	-0.44
Uncertainty Sources	Term [dB]			
$C_{\Gamma_i}^0$ estimation	$\sqrt{\frac{1}{N^2} \sum \sigma_i^2}$	0.03	0.01	0.09
Temp. Corr. in $C_{\Gamma_i}^0$ retrievals	$\frac{\sigma_T}{\sqrt{N}}$	0.05	0.04	0.09
Temp. Corr. in $C_{\Gamma}(T)$, $C_Z(T)$	σ_T	0.13	0.13	0.13
Signal to Clutter Ratio	σ_{SCR}	0.09	0.93	0.09
Bias Correction	σ_{Λ}	0.28	0.05	0.28
Final Calibration Uncertainty	δC_{Γ} ; δC_Z	0.33	0.94	0.35

375 (Delanoë et al., 2016). A Signal to Noise Ratio threshold of 8 dB is used to remove noise samples. We observe that for both campaigns the reflectivity measured in altostratus cloud is within $-30 - 0$ dBZ, which are typical values reported in literature (Uttal and Kropfli, 2001).

7 Conclusions

This study presents a cloud radar calibration method that is based on cloud radar power signal backscattered from a reference
 380 reflector. We study the validity of the method and variability of the results by performing measurements in two experimental

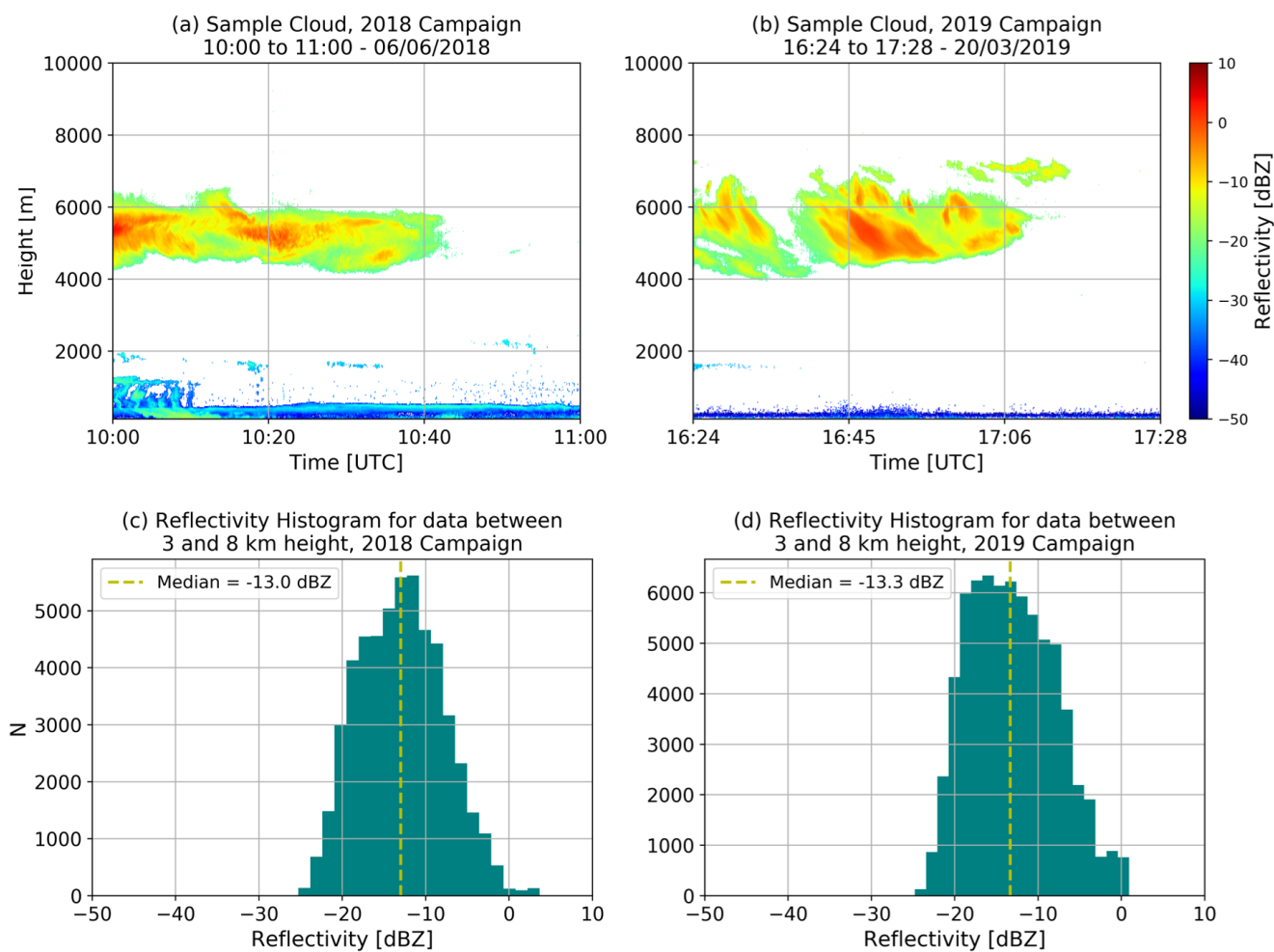


Figure 8. Altostratus cloud sampled during 2018 (a) and 2019 campaigns (b). Lower reflectivities are easier to capture at lower altitudes because of lower distance and attenuation losses (Eq. (3b)). In the altostratus reflectivity histograms (c) and (d) we observe that for both campaigns measurements are within the ranges reported in literature.



setups and analyzing the associated results. In the first experimental setup we use a scanning BASTA-Mini W-band cloud radar, that aims towards a 20-cm triangular trihedral target installed at the top of a 20-m mast, located 376.5 m from the radar. For the second experimental setup, we use the same radar, aimed towards a 10-cm triangular trihedral target mounted on a pan-tilt motor at the top of a 10-m mast. The mast is located 196 m from the radar.

385 The first consideration in the design of the experimental setup is the need to avoid excessive compression or saturation in the radar receiver. This must be checked before any calibration attempt by comparing measurements of radar backscattered power with the radar receiver power transfer curve. In both our setups we find losses due to compression on the order of $0.2 \sim 0.3$ dB. There is a compensating effect between target RCS and radar-to-target distance (Eq. 1b). Since the compression effect is small, we correct it using our receiver power transfer curve. However, in cases where the radar is operating close to saturation,
390 or when compression effects are larger than the calibration uncertainty goal, it is advisable to compensate by reducing target size or by positioning the target further away from the radar.

Secondly, the reflector must be positioned far enough from the radar to be outside the antennas near-field distance and to ensure that the received power has low antenna-overlap losses. The BASTA-Mini cloud radar has a Fraunhofer near-field distance of 50 m. The maximum overlap loss is less than 0.1 dB for the closest (10-m) mast setup. Thus we conclude that the
395 target positioning is far enough for both setups.

Thirdly, the experimental setup should strive to reduce clutter in the radar measurements. This can be achieved by operating in an open field that is several hundred meters in length and free of trees or other signal-inducing obstacles. It is also advisable to perform radar measurements under clear conditions, without fog or rain, with wind speed below 1 ms^{-1} and low turbulence.

Next, the proposed calibration method requires performing several iterations in the same setup configuration. In each iteration the setup is first realigned, followed by approximately one hour of sampling of the reference reflector backscattered
400 power. The sampled power is then corrected for compression effects, incomplete antenna overlap, variations in radar gain due to temperature and atmospheric attenuation, before being used to estimate a RCS calibration term value. Once all iterations are completed, the final RCS and Equivalent Reflectivity calibration terms can be computed with their respective uncertainties.

Iterations are necessary because they enable the quantification of bias introduced by inevitable system misalignment. Our
405 experiments indicate that, for our setup, at least 5 iterations are necessary to reach convergence in the calculation of bias and uncertainty associated with misalignment. We find a bias correction of $\approx 0.4 \pm 0.3$ dB for the 20-m mast, and of $\approx 0.2 \pm 0.1$ dB for the 10-m mast. This difference can be explained by the more precise alignment attainable with the pan-tilt motor installed on the 10 m mast.

Calibration is also impacted by changes in the gain of radar components associated with internal temperature variations.
410 For the radar used in our experiment, these changes reach up to ± 0.6 dB. Our experiments enabled us to retrieve a correction function for the temperature dependence and to reduce the temperature uncertainty contribution to $\sigma_T = 0.13$ dB. This result indicates that lower calibration uncertainties can be achieved by studying temperature effects, especially for solid state radars.

Our analyses reveal that the predominant sources of uncertainty in our experimental setups are due to levels of clutter and alignment precision. These two effects have different magnitudes in our two experimental setups (10-m and 20-m masts). The
415 20-m mast setup uncertainty is limited by the uncertainty contribution of the alignment bias estimation $\sigma_\Lambda = 0.28$ dB. The



10-m mast setup uncertainty is limited by the uncertainty contribution of the signal-to-clutter ratio $\sigma_{SCR} = 0.9 \text{ dB}$. This result reveals that there is a tradeoff between better target alignment and additional clutter introduced by the alignment motor.

The complete uncertainty budget enables us to conclude that the proposed calibration method can yield uncertainties as low as 0.3 dB with our current equipment. This result was obtained using the 20-cm target on the 20 m mast during the 2018
420 experiment, where six target sampling iterations were performed. Additionally, in 2019 two completely different calibration setups were used with the same radar hardware, and in both cases, we obtain the same calibration result within uncertainty bounds.

Finally, because of cloud radar hardware evolutions in the fall of 2018, the calibration coefficients found in May 2018 and March 2019 differ by 1.2 dB . We compare cloud radar measurements of altostratus clouds performed in May 2018 and
425 March 2019. The reflectivity distributions of the two events are consistent and compatible with values previously registered in literature. The two distributions yield median values that differ by 0.3 dB .

For future work we envisage to develop a technological solution to allow target orientation without introducing additional clutter. Another interesting prospect is to improve the accuracy of the radar positioner, to enable direct retrieval of antenna pattern or target RCS directly with the radar instead of relying on laboratory measurements, following the method proposed by
430 Garthwaite et al. (2015).

Further, there is ongoing research on calibration methods based on reference targets held by Unmanned Aerial Vehicles (UAVs) (Yin et al., 2019). Since the underlying principle is the same, most considerations written here should be directly applicable in these new experiments. Here the UAV takes the role of the mast, holding the reflector (usually a sphere), and therefore it is important to characterize the UAV RCS and verify that it does not interfere with the experiment. The main
435 difference would be in the procedure necessary to estimate bias, because the reference target (usually a sphere) will be always moving due to wind. Here an adaptation of the effective RCS simulator would be necessary to account for the target type and different alignment protocol.

Author contributions.

All authors contributed to the planning of the campaigns and the design of the calibration experiments.

440 Author Julien Delanoë was responsible of radar installation and operation.

Authors Jean-Charles Dupont and Felipe Toledo worked in the preparation, development and operation of the necessary infrastructure for the experiments.

Authors Julien Delanoë and Felipe Toledo retrieved the Power Transfer Curve of the Radar Receiver.

Data analysis and the establishment of the calibration methodology presented in the paper was done by Felipe Toledo.

445 Authors Martial Haeffelin and Felipe Toledo worked in defining the paper structure and content.

All authors reviewed the paper.



Competing interests.

Author Felipe Toledo has received research funding from Company Meteomodem.

Acknowledgements. The authors would like to acknowledge Johan Parra, Patricia Delville, Cristophe Boitel and Marc-Antoine Drouin from
450 the SIRTA Atmospheric Observatory for their assistance in the execution of the field experiments. This acknowledgement is extended to
Razvan Pirloaga and Dragos Ene from the INOE Institute, Romania. We would also like to thank Christophe Le Gac, Fabrice Bertrand and
Jean-Paul Vinson from the LATMOS Laboratory, France, for their assistance and the provision of necessary equipment for the experiments.

We also acknowledge the french *Association Nationale de la Recherche (ANRT)* and the company Meteomodem for their contribution in
the funding of this work. Finally, we state this work is part of the ACTRIS-2 project and has received funding from the European Union's
455 Horizon 2020 research and innovation programme under grant agreement No 654109.



References

- Anagnostou, E. N., Morales, C. A., and Dinku, T.: The Use of TRMM Precipitation Radar Observations in Determining Ground Radar Calibration Biases, *Journal of Atmospheric and Oceanic Technology*, 18, 616–628, [https://doi.org/10.1175/1520-0426\(2001\)018<0616:TUOTPR>2.0.CO;2](https://doi.org/10.1175/1520-0426(2001)018<0616:TUOTPR>2.0.CO;2), [https://doi.org/10.1175/1520-0426\(2001\)018<0616:TUOTPR>2.0.CO;2](https://doi.org/10.1175/1520-0426(2001)018<0616:TUOTPR>2.0.CO;2), 2001.
- 460 Atlas, D.: RADAR CALIBRATION, *Bulletin of the American Meteorological Society*, 83, 1313–1316, <https://doi.org/10.1175/1520-0477-83.9.1313>, <https://doi.org/10.1175/1520-0477-83.9.1313>, 2002.
- Bergada, M., Sekelsky, S. M., and Li, L.: External calibration of millimeter-wave atmospheric radar systems using corner reflectors and spheres, *cal*, 3, 6, 2001.
- Boers, R., Baltink, H. K., Hemink, H. J., Bosveld, F. C., and Moerman, M.: Ground-Based Observations and Modeling of the
465 Visibility and Radar Reflectivity in a Radiation Fog Layer, *Journal of Atmospheric and Oceanic Technology*, 30, 288–300, <https://doi.org/10.1175/JTECH-D-12-00081.1>, <https://doi.org/10.1175/JTECH-D-12-00081.1>, 2013.
- Boucher, O., Randall, D., Artaxo, P., Bretherton, C., Feingold, G., Forster, P., Kerminen, V.-M., Kondo, Y., Liao, H., Lohmann, U., et al.: Clouds and aerosols, in: *Climate change 2013: the physical science basis. Contribution of Working Group I to the Fifth Assessment Report of the Intergovernmental Panel on Climate Change*, pp. 571–657, Cambridge University Press, 2013.
- 470 Bringi, V. N. and Chandrasekar, V.: *Polarimetric Doppler weather radar: principles and applications*, Cambridge university press, 2001.
- Brooker, G.: *Sensors and signals*, Citeseer, Australian Centre for Field Robotics, Rose St Building (J04), University of Sydney, Australia, 2006.
- Chandrasekar, V., Baldini, L., Bharadwaj, N., and Smith, P. L.: Recommended calibration procedures for GPM ground validation radars, *GPM Tier1 Documentation Draft*, 9, 2014.
- 475 Delanoë, J., Protat, A., Vinson, J.-P., Brett, W., Caudoux, C., Bertrand, F., Parent du Chatelet, J., Hallali, R., Barthes, L., Haeffelin, M., et al.: Basta: a 95-GHz fmcw doppler radar for cloud and fog studies, *Journal of Atmospheric and Oceanic Technology*, 33, 1023–1038, 2016.
- Doerry, A. W. and Brock, B. C.: Radar cross section of triangular trihedral reflector with extended bottom plate, *Sandia Report*, Sandia National Laboratory, 2009.
- Doviak, R. J. and Zmić, D. S.: *Doppler Radar and Weather Observations*, Mineola, New York: Dover Publications, INC, 2006.
- 480 Dupont, J.-C., Haeffelin, M., Protat, A., Bouniol, D., Boyouk, N., and Morille, Y.: Stratus–fog formation and dissipation: a 6-day case study, *Boundary-layer meteorology*, 143, 207–225, 2012.
- Dupont, J.-C., Haeffelin, M., Wærsted, E., Delanoë, J., Renard, J.-B., Preissler, J., and O’ Dowd, C.: Evaluation of Fog and Low Stratus Cloud Microphysical Properties Derived from In Situ Sensor, Cloud Radar and SYRSOC Algorithm, *Atmosphere*, 9, 169, 2018.
- Ewald, F., Groß, S., Hagen, M., Hirsch, L., Delanoë, J., and Bauer-Pfundstein, M.: Calibration of a 35 GHz airborne cloud
485 radar: lessons learned and intercomparisons with 94 GHz cloud radars, *Atmospheric Measurement Techniques*, 12, 1815–1839, <https://doi.org/10.5194/amt-12-1815-2019>, <https://www.atmos-meas-tech.net/12/1815/2019/>, 2019.
- Fox, N. I. and Illingworth, A. J.: The retrieval of stratocumulus cloud properties by ground-based cloud radar, *Journal of Applied Meteorology*, 36, 485–492, 1997.
- Garthwaite, M. C., Nancarrow, S., Hislop, A., Thankappan, M., Dawson, J. H., and Lawrie, S.: Design of radar corner reflectors for the
490 Australian Geophysical Observing System, *Geoscience Australia*, 3, 2015.
- Haeffelin, M., Barthès, L., Bock, O., Boitel, C., Bony, S., Bouniol, D., Chepfer, H., Chiriaco, M., Cuesta, J., Delanoë, J., et al.: SIRTA, a ground-based atmospheric observatory for cloud and aerosol research, in: *Annales Geophysicae*, vol. 23, pp. 253–275, 2005.



- Haynes, J. M., L'Ecuyer, T. S., Stephens, G. L., Miller, S. D., Mitrescu, C., Wood, N. B., and Tanelli, S.: Rainfall retrieval over the ocean with spaceborne W-band radar, *Journal of Geophysical Research: Atmospheres*, 114, 2009.
- 495 Hogan, R. J., Jakob, C., and Illingworth, A. J.: Comparison of ECMWF winter-season cloud fraction with radar-derived values, *Journal of Applied Meteorology*, 40, 513–525, 2001.
- Liebe, H. J.: MPM—An atmospheric millimeter-wave propagation model, *International Journal of Infrared and millimeter waves*, 10, 631–650, 1989.
- Meissner, T. and Wentz, F. J.: The complex dielectric constant of pure and sea water from microwave satellite observations, *IEEE Transactions on Geoscience and Remote Sensing*, 42, 1836–1849, <https://doi.org/10.1109/TGRS.2004.831888>, 2004.
- 500 Mülmenstädt, J. and Feingold, G.: The radiative forcing of aerosol–cloud interactions in liquid clouds: wrestling and embracing uncertainty, *Current Climate Change Reports*, 4, 23–40, 2018.
- Myhre, G., Shindell, D., Bréon, F. M., Collins, W., Fuglestedt, J., Huang, J., Koch, D., Lamarque, J.-F., and Lee, D.: Mendoza, 25 B, Nakajima, T., Robock, A., Stephens, G., Takemura, T., and Zhang, H. Anthropogenic and natural radiative forcing. In: Stocker, T., Qin, D., Plattner, G.K., Tignor, M., Allen, S., Boschung, J., Nauels, A., Xia, Y., Bex, V., and Midgley, P.(eds) *Climate Change*, 2013.
- 505 Pappalardo, G.: ACTRIS Aerosol, Clouds and Trace Gases Research Infrastructure, *EPJ Web Conf.*, 176, 09 004, <https://doi.org/10.1051/epjconf/201817609004>, <https://doi.org/10.1051/epjconf/201817609004>, 2018.
- Protat, A., Bouniol, D., Delanoë, J., O'Connor, E., May, P. T., Plana-Fattori, A., Hasson, A., Görsdorf, U., and Heymsfield, A. J.: Assessment of CloudSat reflectivity measurements and ice cloud properties using ground-based and airborne cloud radar observations, *Journal of Atmospheric and Oceanic Technology*, 26, 1717–1741, 2009.
- 510 Protat, A., Bouniol, D., O'Connor, E. J., Klein Baltink, H., Verlinde, J., and Widener, K.: CloudSat as a Global Radar Calibrator, *Journal of Atmospheric and Oceanic Technology*, 28, 445–452, <https://doi.org/10.1175/2010JTECHA1443.1>, <https://doi.org/10.1175/2010JTECHA1443.1>, 2011.
- Scolnik, M. I.: *Radar Handbook*, Mc Craw-Hill, 3 edn., 2000.
- 515 Sekelsky, S. M. and Clothiaux, E. E.: Parallax Errors and Corrections for Dual-Antenna Millimeter-Wave Cloud Radars, *Journal of Atmospheric and Oceanic Technology*, 19, 478–485, [https://doi.org/10.1175/1520-0426\(2002\)019<0478:PEACFD>2.0.CO;2](https://doi.org/10.1175/1520-0426(2002)019<0478:PEACFD>2.0.CO;2), [https://doi.org/10.1175/1520-0426\(2002\)019<0478:PEACFD>2.0.CO;2](https://doi.org/10.1175/1520-0426(2002)019<0478:PEACFD>2.0.CO;2), 2002.
- Uttal, T. and Kropfli, R. A.: The Effect of Radar Pulse Length on Cloud Reflectivity Statistics, *Journal of Atmospheric and Oceanic Technology*, 18, 947–961, [https://doi.org/10.1175/1520-0426\(2001\)018<0947:TEORPL>2.0.CO;2](https://doi.org/10.1175/1520-0426(2001)018<0947:TEORPL>2.0.CO;2), [https://doi.org/10.1175/1520-0426\(2001\)018<0947:TEORPL>2.0.CO;2](https://doi.org/10.1175/1520-0426(2001)018<0947:TEORPL>2.0.CO;2), 2001.
- 520 Wærsted, E. G., Haeffelin, M., Dupont, J.-C., Delanoë, J., and Dubuisson, P.: Radiation in fog: quantification of the impact on fog liquid water based on ground-based remote sensing, *Atmospheric Chemistry and Physics*, 17, 10 811–10 835, <https://doi.org/10.5194/acp-17-10811-2017>, <https://www.atmos-chem-phys.net/17/10811/2017/>, 2017.
- Wærsted, E. G., Haeffelin, M., Steeneveld, G.-J., and Dupont, J.-C.: Understanding the dissipation of continental fog by analysing the LWP budget using idealized LES and in situ observations, *Quarterly Journal of the Royal Meteorological Society*, 145, 784–804, <https://doi.org/10.1002/qj.3465>, <https://rmets.onlinelibrary.wiley.com/doi/abs/10.1002/qj.3465>, 2019.
- 525 Yau, M. K. and Rogers, R. R.: *A short course in cloud physics*, Elsevier, 1996.
- Yin, J., Hoogeboom, P., Unal, C., Russchenberg, H., Van der Zwan, F., and Oudejans, E.: UAV-Aided Weather Radar Calibration, *IEEE Transactions on Geoscience and Remote Sensing*, 57, 10 362–10 375, <https://doi.org/10.1109/TGRS.2019.2933912>, 2019.